Time-resolved Biofilm Deformation Measurements using Optical Coherence Tomography

Florian Blauert[1,*], Harald Horn[1], and Michael Wagner[1,2]

[1]Chair of Water Chemistry and Water Technology, Karlsruhe Institute of Technology, Engler-Bunte-Ring 1, D-76131 Karlsruhe, Germany

[2]Institute of Functional Interfaces, Karlsruhe Institute of Technology, Hermann-von-Helmholtz-Platz 1, D-76344 Eggenstein-Leopoldshafen, Germany

[*]Corresponding author: Florian Blauert, Chair of Water Chemistry and Water Technology, Karlsruhe Institute of Technology, Engler-Bunte-Ring 1, D-76131 Karlsruhe, Germany, telephone: +49(0)72160846379, fax: +49(0)72160846497, e-mail: florian.blauert@kit.edu

Abstract

The interaction of shear stress with the biofilm leads to a dynamic deformation, which is related to the structural and material characteristics of biofilms. We show how optical coherence tomography can be used as an imaging technique to investigate the time-resolved deformation on the biofilm mesoscale as well as to estimate mechanical properties of the biofilm. For the first time time-resolved deformation from cross-sectional views of the inner biofilm structure could be shown. Changes in the biofilm structure and rheological properties were calculated from cross sections in real time and time-lapsed measurements. Heterotrophic biofilms were grown in a flow cell set-up at low shear stress of $\tau_w = 0.01$ Pa. By applying higher shear stress elastic and viscoelastic behavior of biofilms were quantified. Deformation led to a change in biofilm conformation and allowed to estimate rheological properties. Assuming an ideal wall shear stress calculation, the shear modulus $G = 29.7 \pm 1.7$ Pa and the Young's modulus $E = 36.0 \pm 2.6$ Pa were estimated.

Keywords: optical coherence tomography, biofilm rheology, mechanical properties, time-resolved deformation, shear and Young's modulus, mesoscale.

Introduction

Microbial communities form biofilms, which are attached to interfaces. Such systems typically grow in moist environments and consist of several species partly forming cell clusters, which are embedded in a matrix of extracellular polymeric substances (EPS, Flemming and Wingender, 2010). As the size of the involved microorganisms is in the range of micrometers, microscopic techniques have been applied to describe biofilm structures since the early 1990's (Lawrence et al., 1991). Nevertheless, in recent years the mesoscale (range of mm) of biofilm structures has been identified as important part for the understanding of biofilm systems (Morgenroth and Milferstedt, 2009). Especially the behavior of biofilm structures under certain hydrodynamic (shear) conditions could only be understood better if the mechanical properties of the viscoelastic material are known (Böl et al., 2013; Guélon et al., 2011). The viscoelastic behavior of biofilms results in a reduced effectivity if increased shear stress is applied to remove parts of the biofilm (Rupp et al., 2005). Biofilms which adapted to the stresses in their growth environment are able to withstand a variety of changing conditions (e.g. toxins, oxidants, or disinfection) due to the protective properties of the biofilm matrix (Brooun et al., 2000; Spoering and Lewis, 2001; Yoo and Chen, 2012). Stress induced detachment seems to be an alternative cleaning procedure where the flow velocity is simply changed to create a change in shear stress. Therefore it is essential to investigate the ability of biofilms to withstand erosion and sloughing, i.e. to understand the mechanical behavior. Biofilm rheology deals with the physical properties of the biofilm matrix which depend on the composition of the EPS and influences the shape as well as mechanical stability of biofilms (Christensen and Characklis, 1990; Klapper et al., 2002). Investigations of biofilm rheology were mainly done by either microscopic techniques such as light and fluorescence microscopy (Klapper et al., 2002;

53 Stoodley et al., 1999) or macroscopic techniques such as compression measurements (Körstgens et
54 al., 2001), rheometer creep analysis (Towler et al., 2003), and fluid dynamic gauging (Möhle et al.,
55 2007). While microscopic techniques investigate biofilm structures on a scale of approximately
56 hundred μm to reveal structural dynamics, macroscopic techniques use much larger structures to
57 measure average rheological properties. To validate measured quantities on micro- and macroscale,
58 a technique to measure on the scale in between needs to be applied. A technique capable to resolve
59 structures in the mm-range with a μm resolution is optical coherence tomography (OCT). OCT is
60 a technique to measure depth-resolved reflection signals from translucent samples such as biofilms
61 (Huang et al., 1991). Advantages over conventional imaging techniques used for structural
62 description, such as confocal laser scanning microscopy (CLSM), are the fast measurement speed,
63 no need for staining, and the possibility to measure *in situ* without destroying the biofilm structure.
64 OCT can additionally be used as tool to analyze biofilm characteristics such as porosity, roughness
65 and distribution of cavities (Wagner et al., 2010; Xi et al., 2006). Recently, OCT has been used for
66 the on-line observation of biofouling in membrane fouling simulators to investigate the biofouling
67 behavior in reverse osmosis and nanofiltration systems (Dreszer et al., 2014).
68 In the present study we demonstrate the implementation of OCT to image biofilm deformation
69 under non-stationary conditions. Experiments for dynamic and time-lapsed analysis of biofilm
70 behavior adapting to changing shear stress conditions have been conducted. The technique
71 developed allowed to follow structural changes of biofilms at the mesoscale in time-resolved
72 measurements of two-dimensional cross sections as well as in volumetric datasets. A subsequently
73 performed digital image analysis was used to estimate rheological parameters. Thereby, the
74 dynamic change of the biofilm structure could be related to the applied shear stress.

Materials and Methods

Biofilm Cultivation

For each experiment a biofilm was grown in a transparent flow cell with a straight channel made of poly-methyl-methacrylate (PMMA, channel dimensions ($L \times W \times H$): $124 \times 2 \times 1$ mm^3) as shown in Figure 1 A. A bubble trap (Technical University of Denmark, Department of Systems Biology, Lyngby, Denmark) was installed between peristaltic pump (Ecoline VC-MS/CA8-6, Ismatec, Weinheim, Germany) and flow cell in order to avoid gas bubbles entering the flow cell and to compensate for pulsation of the flow. All components were connected with silicone rubber tubing. The flow cell was inoculated for 24 h with 20 ml of activated sludge supernatant (KA Neutreut, Karlsruhe, Germany). After the inoculation phase the system was changed to a flow through set-up by which the suspended bacteria were washed out of the system. The cultivation medium was composed of (inflow concentration in mg/L): $(NH_4)_2SO_4$ (18), $MgSO_4 \cdot 7H_2O$ (13), $NaNO_3 \cdot 2H_2O$ (12), $CaCl_2 \cdot 2H_2O$ (9), and $FeSO_4 \cdot 7H_2O$ (10). Glucose (30 mg/L) was chosen as sole carbon source and trace elements were added (in µg/L): H_3BO_3 (300), $CoCl_2 \cdot 6H_2O$ (110), $MnSO_4 \cdot H_2O$ (20), $Na_2MoO_4 \cdot 2H_2O$ (26), $NiCl_2 \cdot 6H_2O$ (10), and $ZnSO_4 \cdot 7H_2O$ (56). The solution was phosphate buffered to keep pH = 6.8.

Optical Coherence Tomography

A spectral domain optical coherence tomograph (GANYMEDE, Thorlabs GmbH, Dachau, Germany) was used to visualize biofilm structure in shear stress experiments. Optical coherence tomography (OCT) measures intensity depth profiles (A-scan) from translucent samples such as biofilms. Consecutive A-scans provide a cross-sectional view of the biofilm structure (B-scan, xz-

plane). B-scans are combined to volumetric representations within this communication referred to as C-scan. In Figure 1 B the OCT principle is shown. Briefly, a broadband super luminescent diode (SLD) with a central wavelength of 930 ± 80 nm is used as light source in a Michelson interferometer. The light is split at the beam splitter into the reference and the sample arm. Through the sample arm the light penetrates the sample and is reflected. The reflected light superimposes with the light from the reference arm and creates an interference pattern. This interference pattern is transformed via a fast Fourier transformation (FFT) into a depth-resolved intensity signal for one spot (A-scan, z-direction) to generate a depth profile. By scanning along the x-dimension a 2D cross section through the biofilm structure is generated (B-scan, xz-plane). By acquiring consecutive B-scans along the y-dimension a volumetric representation is created (C-scan). The scanning speed of the OCT used in this study reaches up to 29000 A-scans/s and covers a lateral field of view of 10 × 10 mm^2. With a maximal axial resolution of <5.8 µm and 8 µm lateral, OCT is capable to visualize whole 3D structures in seconds.

Shear Stress Experiments

To allow a better understanding of the performed experiments, it has to be stated that the term 'dynamic' is used for experiments in which the time between consecutive B-scans is short compared to the time it takes to acquire a single C-scan. In 'time-lapsed' experiments the time between consecutive acquired B- or C-scans is much longer compared to the acquisition time of a single B- or C-scan. In consequence, time series of cross sections (B-scans) can be dynamic or time-lapsed, whereas volumetric representations (C-scans) are always time-lapsed measurements.

For shear stress experiments biofilms were grown in the flow cell as described earlier in Materials and Methods. The effect of a raised shear stress was studied on biofilm structures developed in the center of the flow channel. The investigated structures were either round and patchy or flat and streamer-like shaped. The OCT was set to measure B-scans (xz-cross sections) along the flow in the center of the flow channel (see Fig. 1 A) to reveal the inner structure of the biofilm and its change during deformation. The changes in biofilm conformation were measured by suddenly increasing the shear stress. The OCT scan rate was set to 10000 A-scans/s for enhanced image quality, acquiring B-scans (xz-cross sections) of 2.00×1.95 mm^2 (1024 pixel × 700 pixel, px^2) within 100 ms (10 frames per second, fps). Each acquired B-scan consisted of 1024 A-scans. In a first shear stress experiment the deformation of the biofilm was induced by applying an elevated shear stress for a duration of 10 s. This experiment was conducted to estimate the time needed to reach the maximal deformation of the biofilm. A more detailed experiment was conducted to relate the change of the biofilm structure to the changed shear stress conditions. Therefore, a series of 22 B-scans was acquired over 2.1 s providing accurate imaging of the biofilm deformation on-line and *in situ*. Flow cell hydrodynamics were calculated according to Stoodley et al. (2001) assuming fully developed laminar flow through a rectangular flow channel.

The hydraulic diameter D_h was derived from the width (W) and height (H) of the flow channel:

$$D_h = \frac{4HW}{2(H+W)} \quad (1)$$

The maximal flow velocity in the flow cell can be approximated from the average flow velocity u_{avg} as follows:

$$u_{max} = \frac{3}{2} u_{avg} \quad (2)$$

The Reynolds number *Re* has been calculated according to:

$$Re = \frac{u_{avg}\, D_h}{\nu} \quad (3)$$

where ν is the kinematic viscosity of water at 20°C.

The wall shear stress τ_w was calculated from the dynamic viscosity of water η, the maximal flow velocity in the flow cell u_{max} and the hydraulic diameter D_h:

$$\tau_w = \frac{4\eta u_{max}}{D_h} \quad (4)$$

Here it needs to be stressed that the wall shear stress τ_w was calculated assuming an ideal fully developed laminar flow between infinite parallel plates. Therefore τ_w does not account for local disturbances of the fluid flow by the heterogeneity of the biofilm structure and movement of the biofilm itself. In consequence estimates of moduli can be considered approximate, but allow comparison with existing values (i.e. Stoodley et al., 1999).

The shear modulus *G* was estimated from the angle of deformation α from the OCT B-scans before and after changing the shear stress τ_w:

$$G = \frac{\tau_w}{\alpha} \quad (5)$$

Stress-Strain Experiments

Stress-strain experiments were conducted by incrementally increasing (load cycle) or decreasing the shear stress (unload cycle). Stress-strain experiments were performed at shear stress level of $\tau_w = 0.04$ (growth condition), 0.43, 0.82, 1.21, 1.61, 2.00, 2.39, 2.78, 3.17, and 3.56 Pa, respectively. The shear stress was applied for 60 s onto the biofilm structure before an OCT C-scan was acquired. The C-scan volume of $3.00 \times 3.00 \times 1.46\ mm^3$ ($350 \times 350 \times 700\ voxel$) was acquired within 12 s capturing the volumetric representation of the biofilm. The elongation of biofilm structures due to applied shear stresses was quantified from single cross sections (B-scans) of the C-scan. Strain ε was calculated from the change in length Δl relative to the length l of the biofilm structure (imaged at no flow):

$$\varepsilon = \frac{\Delta l}{l} \quad (6)$$

The Young's Modulus E was estimated from the linear part of the load cycle in the resulting stress-strain curve:

$$E = \frac{\tau_w}{\varepsilon} \quad (7)$$

Image Analysis

OCT data sets were processed using ImageJ 1.48u (Schneider et al., 2012). For image processing B-scans were cropped to the minimal size possible without losing biofilm related information. An

implemented plugin ("Find Connected Regions") was used to identify connected biofilm structures. *Otsu's* method was used to threshold and binarize the B-scans (Otsu, 1979). The elongation ΔL of the biofilm structure and the angle of deformation α were calculated from manual displacement measurements, while the mean biofilm thickness $\bar{L}_F$ and porosity were processed by in-house macros. The following parameters were used to describe and characterize changes in the biofilm structure:

Mean Biofilm Thickness

The mean biofilm thickness of each OCT B-scan was calculated from:

$$\bar{L}_F = \frac{1}{N}\sum_{i=1}^{N} L_{F,i} \tag{8}$$

where $L_{F,i}$ is the biofilm thickness from a single A-scan i in the corresponding B-scan and N is the total number of A-scans. Mean biofilm thickness was calculated for each OCT B-scan either in a series of B-scans or in C-scans offering the possibility to monitor the change (e.g. compression) during the experiment.

Surface Roughness Coefficient

The surface roughness coefficient of the biofilm was calculated according to Murga et al. (1995):

$$R_a^* = \frac{1}{N}\sum_{i=1}^{N} \frac{|L_{F,i} - \bar{L}_F|}{\bar{L}_F} \tag{9}$$

where i represents a particular A-scan and N the overall number of A-Scans. Biofilms with a smooth surface and only few variations from the mean biofilm thickness have low values close to zero. The

higher the roughness coefficient, the more variations are expected from the biofilm surface structure.

Biofilm Porosity

The biofilm porosity $\Phi_{biofilm}$ is the ratio of background to foreground signals. Within this study the biofilm porosity excludes background signals outside the biofilm structure. Biofilm porosity is thus the ratio of void signals only within the biofilm and the total area of the biofilm containing both, biomass and voids or cavities. This parameter has already been used to characterize the structure of different biofilms imaged by means of OCT cultivated under different hydrodynamic flow conditions (see Wagner et al., 2010).

$$\Phi_{biofilm} = \frac{A_{voids}}{A_{biofilm}} = \frac{A_{voids}}{A_{biomass}+A_{voids}} \quad (10)$$

A decline of the biofilm porosity can be interpreted as reduction of void space and thus quantify the compression behavior of the biofilm.

Results

Mechanical properties of biofilms grown under similar conditions were investigated in dynamic and time-lapsed deformation experiments at different shear stress levels. It is important to notice here, that dynamic experiments evaluate changes in 'real' time while time-lapsed experiments were conducted to measure the viscoelastic behavior of biofilms.

Dynamic Biofilm Deformation

In dynamic deformation experiments the impact of a changing flow velocity and shear stress on the biofilm structure was investigated in two experiments. In the first experiment different shear stress levels were applied for 10 s and the corresponding deformation was recorded in a series of B-Scans (see suppl. material, videos 1 and 2). By setting the initial shear stress to growth conditions (Re = 4) no compression or deformation was detected compared to no flow conditions. At higher shear stresses of τ_w= 0.3, 0.6, and 0.8 Pa (*Re* = 91, 172, and 250, respectively) the biofilm showed a deformation/compression along the flow (x-axis). In Figure 2 exemplarily the deformation at $\tau_w =$ 0.6 Pa is shown after 0, 2, and 10 s, respectively. Due to the patchy biofilm structure, the front section of the biofilm got visibly compressed. The biofilm porosity decreased during the experiment by 2% to a value of 45% and fully recovered to 47% when the shear stress was reduced to the cultivation level. The maximal compression of the biofilm (measured in Figure 2 as distance between the left side of the B-scan and the biofilm) reached 148 µm after 2 s. After these 2 s no further compression or change was detected until the flow was stopped. Further increased shear stress did not force a stronger compression. Thereby, it was validated that deformation happens within the first seconds after the increase of the shear stress. Since the biofilm detached partly from the substratum during the deformation experiments and finally sloughed off at a shear stress of 1.1 Pa, a biofilm grown in another flow cell has been investigated to assess mechanical properties.

A more detailed insight into the deformation process of the first two seconds was gained in a second experiment from a biofilm completely attached to the substratum. This experiment was conducted at a Reynolds number of *Re* = 485 resulting in a shear stress of $\tau_w = 1.64$ Pa. The deformation process was monitored for 2.1 s by acquiring a series of B-scans (see Materials and Methods). The

231 deformation behavior is illustrated in Figure 3. The last image at 2100 ms (white line represents
232 the original structure at 0 ms) indicates the necessity to differentiate the observed biofilm structure
233 into two parts, since a different deformation for the upstream and downstream part of the biofilm
234 was observed. The upstream part showed a large deformation in the first half of the image. For the
235 downstream part of the visualized biofilm a smaller deformation was detected and a filamentous
236 structure showed an elongation caused by the constant stress.
237 The mean biofilm thickness of the whole structure under growth conditions (τ_w = 0.01 Pa) equaled
238 $\bar{L}_F = 420$ µm. The development of the mean biofilm thickness is presented in Figure 4. Increasing
239 the shear stress to τ_w = 1.64 Pa resulted in deformation and a reduction of biofilm thickness. Within
240 400 ms (see Figures 4 and 3, B-scans 200 − 600 ms) the mean biofilm thickness was reduced to
241 $\bar{L}_F = 408$ µm. The mean biofilm thickness of the total structure showed a plateau between B-scans
242 captured at 600 ms and 1300 ms indicated by the grey area in Figure 4 A. The cause for the plateau
243 region can be understood by dividing the image in a front and rear half and investigating the
244 changes of the mean biofilm thickness separately. The calculated mean biofilm thickness for the
245 upstream (front half, filled circle •) and downstream part (rear half, empty circle ◦) of the biofilm
246 structure showed different trends. The front half showed a steady decrease of the mean biofilm
247 thickness, while the rear half kept increasing with a fluctuation between 1500 and 1700 ms. The
248 mean biofilm thickness of the complete biofilm structure decreased after the plateau to $\bar{L}_F =$
249 394 µm and the average biofilm thickness reduction/compression was $\Delta\bar{L}_F = 27$ µm; ≈ 6 % of the
250 initial mean biofilm thickness. From the structure geometry it is expected that the flow by-passed
251 the rear half of the biofilm causing less changes there as seen in Figure 3 and Figure 4. The
252 filamentous structure at the biofilm surface started to elongate shortly after the shear stress was

raised until the end of the experiment (B-scans 400 – 2100 ms, see Figure 3). The maximal elongation detected was ΔL = 220 µm. This was quite large but to be expected for biofilms investigated at the mesoscale. During the experiment the filament oscillated perpendicular to the scan axis, which caused intensity variations and influenced the mean biofilm thickness (see decrease of $\bar{L}_F$ after 1.5 s for the downstream part in Figure 4 A). The surface roughness coefficient also increased over the experimental duration. The development of the surface roughness coefficient is presented in Figure 4 B. By setting the shear stress to τ_w = 1.64 Pa, the surface roughness coefficient rose from $R_a^* = 0.177$ to $R_a^* = 0.245$ (see Figure 4 B). At the beginning of the plateau in the mean biofilm thickness curve (see Figure 4 A, B-scan at 600 ms) the slope of the roughness coefficient decreased (see gray highlighted area in Figure 4 B). Subsequent compression did not influence the slope further. At 1600 ms in Figure 4 B an artificial increase was observed. This was due to by-passing biomass causing a 'shadowing effect' which in turn led to an underestimation of the mean biofilm thickness and overestimation of the surface roughness, respectively.

The intensity of the shear stress caused the front of the biofilm structure to bend and deform. The comparison of the beginning and the end of the experiment is presented in Figure 5. From the cross-sectional views (B-scans) the overall structure appeared intact and no detachment was detected. For the particular biofilm structure OCT did not allow to acquire all signals. Especially, signals from deeper regions and the bottom of the biofilm are missing in Figure 5. These regions appear black and it was not possible to distinguish between cavities/voids and signal depletion. For the investigated structure a decrease of the biofilm porosity $\Delta\Phi_{biofilm}$ = 2% was calculated over the entire experiment with a biofilm porosity $\Delta\Phi_{biofilm}$ ranging from 66 to 64 %. As described in the

Materials and Methods section, the angle of deformation can be used to estimate the shear modulus G. In Figure 5 A the B-scan of undeformed biofilm is shown. The straight white line thereby marks the position of the biofilm before the deformation at τ_w = 1.64 Pa. The measured change in the angle of deformation was estimated to be $\alpha = 3°$. Assuming a minimum uncertainty of 1 pixel (or 8.6 µm) with respect to the positioning of the line at the biofilm structure used to measure the angle of deformation, a shear modulus of G = 31.3 ± 0.5 Pa was estimated for this single shear stress experiment.

Time-Lapsed Biofilm Deformation

A biofilm was exposed in a time-lapsed experiment to a shear stress of $\tau_w = 1.64$ Pa for 30 min followed by a relaxation of 20 min wherein no shear stress was applied. OCT B-scans were acquired to quantify structural parameters (angle of deformation, the biofilm porosity, etc.) as well as to calculate mechanical characteristics of the biofilm (shear modulus G, strain ε). In Figure 6 a set of four B-scans shows the deformation and recovery properties of the biofilm. The location of the B-scan in relation to the flow cell was constant between the visualization after 0, 1, 30, and 50 min. As shown in Figure 6 the biofilm reached a maximal angle of deformation of $\alpha = 3°$ within the first OCT scan after 1 min and kept the deformation until the applied shear stress was removed. The biofilm in the time-lapsed measurement showed similar behavior compared to the dynamic deformation experiments described in the previous section. Again, from the deformation over time a shear modulus of G = 29.7 ± 1.7 Pa (n=10) was estimated confirming the results of the shear stress experiments. After the flow was stopped, the biofilm showed an elastic response by returning into its original position.

Additional stress-strain experiments were conducted to assess the viscoelastic properties of biofilm grown in the flow cell. Therefore, C-scans were acquired to follow the deformation and recovery of the biofilm structure. Briefly, shear stress was incrementally increased in a load cycle and decreased in an unload cycle ranging from $\tau_w = 0 - 3.6$ Pa ($\Delta\tau_w = 0.4$ Pa, $Re = 0 - 1000$). Shear stress was kept constant for 1 min before OCT C-scans were acquired. The change of the internal volumetric biofilm structure was estimated by analyzing the each B-scans of the corresponding C-scan. The volumetric porosity development is shown in Figure 7 A and decreased during the load cycle by $\Delta\Phi_{biofilm} \approx 7$ % from $\Phi_{biofilm} = 51 \pm 12$ % to 43 ± 10 % (see Figure 7 A). During the unload cycle the porosity dropped slightly by approximately 1 % and remained then constant at a level of $\Phi_{biofilm} = 43 \pm 10$ % until a shear stress of $\tau_w = 1.6$ Pa was reached. A further decrease of the shear stress increased the biofilm porosity to $\Phi_{biofilm} = 46 \pm 10\%$. Due to erosion the biofilm porosity dropped at $\tau_w = 2$ Pa during the loading cycle. The surface roughness coefficient R_a^* of the volumetric representation showed a similar behavior and is presented in Figure 7 B. It kept decreasing in the load cycle ($R_a^*(0\text{ Pa}) = 0.58 \longrightarrow R_a^*(3.6\text{ Pa}) = 0.55$) and increasing in the unload cycle ($R_a^*(3.1\text{ Pa}) = 0.535 \longrightarrow R_a^*(0\text{ Pa}) = 0.57$). During the load cycle a relatively large change of the roughness coefficient occurred at a shear stress of $\tau_w = 1.2$ and 2.4, respectively. In the unload cycle the recovery of the surface roughness coefficient was quite smooth. In Figure 8 an OCT B-scan of the biofilm is shown at no load conditions ($\tau_w = 0$ Pa). The white line represents the structure before the load cycle. It displays the structural change between the beginning and end of the experiment at $\tau_w = 0$ Pa. After the experiment the structure did not regain its original shape as to be expected for a viscoelastic behavior of biofilms. At the upstream part the biofilm structure is deformed while at the rear part erosion occurred.

To characterize the viscoelastic behavior of the biofilm in more detail, the mean biofilm thickness and the strain were calculated for the biofilm structure present in the center B-scan of the corresponding C-scan acquired at the different shear stress level. In Figure 9 A the mean biofilm thickness is related to the shear stress. The mean biofilm thickness decreased from $\bar{L}_F = 220$ to 160 µm corresponding to an average compression of 27%. During the first four changes of shear stress in the load cycle the mean biofilm thickness decreased as a result only of the compression of the biofilm structure. At $\tau_w = 1.2$ Pa detachment occurred followed by a reduced slope in the mean biofilm thickness curve. During the unload cycle the mean biofilm thickness kept increasing until $\bar{L}_F = 175$ µm. This corresponds to 80 % of the initial mean biofilm thickness of 220 µm. The unload cycle thereby revealed the viscoelastic behavior of biofilms. Furthermore, strain was calculated based on the center B-scans and linked to the shear stress in a stress-strain curve. The stress-strain correlation is given in Figure 9 B. In the load cycle the applied shear stress correlated linearly to the resulting strain. Fitting a linear function to the data allowed for extraction of the slope and the calculation of the Young's Modulus E. The Young's Modulus E was estimated to equal $E = 36.0 \pm 2.6$ Pa (r^2=0.97, n=3). During the unload cycle a hysteresis was detected and no clear correlation between applied shear and strain could be estimated. The results prove the viscoelastic characteristics of the analyzed biofilm.

Discussion

By suddenly changing the volumetric flow to vary shear stress, the behavior of biofilm structures under these changed conditions was investigated. Therefore, series of B-scans (2D) and C-scans

(3D) have been acquired at the mesoscale, respectively. The imaging datasets were analyzed to characterize structural as well as mechanical properties of biofilms in more detail.

We demonstrate the application of OCT to investigate dynamics of the biofilm structure in shear stress and stress-strain experiments without the necessity of a sample preparation, non-invasively, *in situ*, and fast. The results presented in the current study allowed to follow the initial dynamics and in addition reveal elastic and viscoelastic properties of mesoscopic biofilm structures. The results of image analysis can further be used for a qualitative and quantitative interpretation of biofilm rheology.

Dynamic Processes

Exposing biofilms to different shear stress levels showed that it took approximately 2 seconds for the biofilm to adapt to new shear stress conditions by deformation (compression and elongation). He *et al.*, (2013) showed, that according to the Maxwell model, the viscoelastic behavior of biofilms can be described by three stress relaxation processes, each with a characteristic time-constant. The fastest process corresponds to water extrusion and occurs within the first few seconds during externally applied load. The other two relaxation processes were related to the rearrangement of biofilm constituents (e.g., EPS) occurring between 5 to 100 s after the load was created. The rearrangement of bacteria within the deformed biofilm occurs when the load is applied for more than 100 s. This coincides well with the initial deformation behavior found in the shear stress experiments conducted in this study at different shear stress levels. Within the time frame of 2 s the biofilm either compressed/deformed (see suppl. material, video 1) or detached (see suppl. material, video 2). The whole biofilm adapts quickly to the invoking stress, while the largest compression can be measured in the upstream part of the biofilm structure. After the adaption phase no change

in the position of the biomass or voids was detected until the flow was stopped. The behavior seems to be plausible due to fact that the upstream part of the biofilm faces the strongest forces as shown for biofilm streamers by Taherzadeh et al. (2010). For the 10 s of applied shear stress no creep was expected and the biofilm returned to its initial shape. For the highest shear stress applied in the first shear stress experiment ($\tau_w = 1.1$ Pa) the biofilm detached after an adaption phase and finally sloughed off within two B-scans ($\Delta t \approx 250$ ms, see suppl. material, video 2). Because the A-scan rate was set to 10000 s^{-1} for an enhanced imaging quality, it was not possible to follow the detachment and sloughing in more detail. Setting the A-scan rate to 30000 s^{-1} could allow for the visualization of detachment processes. There are OC tomographs available, which provide A-scan rates up to approximately 10^5 s^{-1} and thus could possibly follow erosion and sloughing (Drexler and Fujimoto, 2008).

Nevertheless, further insights into the dynamics of the biofilm structure were revealed from shear stress experiments. The advantages of OCT over other imaging modalities to follow a biofilm deformation (i.e., stereo microscopy as shown by (Stoodley et al., 1999)) are obvious since in addition to the deformation the change in the biofilm thickness, porosity, and surface roughness were revealed.

The analysis of the biofilm thickness development after the shear stress was set to $\tau_w = 1.64$ Pa shows the strength of the imaging by means of OCT. Between 600 – 1300 ms the mean biofilm thickness reached a plateau (see Figure 4 A). In more detail it was shown that for the upstream part of the biofilm structure the mean biofilm thickness kept decreasing, whereas the downstream part showed a slight increase. This is the result of two effects. One concerns the elongation of the upper filamentous structure, which causes the mean biofilm thickness to rise, and the second effect is the

383 elastic expansion perpendicular to the flow caused by the compression along the flow (see Figure
384 3). This is known for elastic materials and the Poisson's ratio provides a number for this behavior.
385 While elongation of the biofilm continued until the shear stress experiment finished, the mean
386 thickness kept decreasing, indicating that elongation did not compensate totally for the compression
387 (see Figure 4 A). Especially the base of the filamentous structure, which was pushed downstream,
388 enhanced the mean biofilm thickness of the downstream part. These effects compensated for the
389 decrease of the mean biofilm thickness of the upstream part, yielding a steady mean biofilm
390 thickness of the complete structure. This was further supported by the change of the surface
391 roughness coefficient. The constant rise of the roughness coefficient during the plateau phase
392 indicated that the biofilm structure was compressed unequally over its length. The deformation of
393 the upstream surface led to a reduced biofilm thickness compared to the downstream part. Hence,
394 the variation of the local biofilm thickness compared to the mean biofilm thickness increased;
395 consequently the roughness coefficient increased, too.
396 A limitation of the acquisition of cross-sectional views (B-scans) is the movement of biofilm out
397 of the imaging plane during data collection. For example oscillation of the filamentous part of the
398 biofilm caused the structure to bend/move out of the B-scan. This led to signal depletion especially
399 in measurements under dynamic flow conditions. As a consequence the OCT lost biomass-related
400 signals explaining the drop at 1600 ms in the mean biofilm thickness curve for the downstream part
401 of the biofilm in Figure 4 A. Another consequence was a variation of the surface roughness
402 coefficient as seen in Figure 4 B. Similar signal depletion can occur due to detachment. OCT is
403 sensitive for particles blocking the light path (Haisch and Niessner, 2007). Biomass flushed through
404 the flow channel scatters the light rather than reflects it, causing the depletion of signal as shown
405 in Figure S1. Scattering can cause problems in time-resolved measurements and might create data

406 variations influencing the quality of calculated structural parameters. To reduce the impact of such
407 imaging artifacts averaging of A- or B-scans can be acquired with the drawback of prolonged
408 measurement time.
409 In Figure 5 the elongation determination of the biofilm structure is illustrated. The measured
410 elongation of the filamentous structure was 220 µm and is as large as whole biofilm structures
411 reported from other rheological studies by Klapper et al. (2002) or Stoodley et al. (1999). Stoodley
412 et al. (1999) conducted similar flow cell experiments on the microscale with biofilm streamers
413 grown at high shear stress (τ_w = 3.6 Pa). They used light microscopy to determine the angle of
414 deformation and elongation of the structure as well as applied fluorescent particles to calculate
415 strain. The limitations of such experiments are on the one hand the size of the biofilm structure of
416 only a few hundred µm due to the restricted field-of-view of microscopes and on the other hand the
417 restriction of the visualization to the surface structure of the biofilm (xy-cross section) rather than
418 the xz-cross sections (2D) or C-scans (3D) acquired by means of OCT. Of course one could add
419 fluorescent particles, which are embedded into the biofilm structure and their displacement is tried
420 to follow by means of stereo-microscopy imaging (Hu et al., 2013); somehow similar to the impact
421 of the nanoparticle size onto their diffusion in biofilms (Peulen and Wilkinson, 2011). Nevertheless,
422 with microscopic techniques it is still not possible to describe validly the cavity distribution or
423 reveal dynamics inside the biofilm without manipulation the structure. In the experiments of
424 Stoodley et al. (1999) an effective shear modulus of $G = 27.1 \pm 0.9$ Pa was measured, which is
425 close to the findings of this study of an average shear modulus of $G = 29.7 \pm 1.7$ Pa. Despite the
426 size difference the biofilms indicated similar rheological behavior compared to the experiments
427 presented in the current study.

Another technique to describe biofilm morphology on the microscale is atomic force microscopy (AFM). AFM is a powerful technique to image the biofilm surfaces at nanometer resolution. The technique is often used to investigate single cell attachment onto substrata or interfaces (Beech et al., 2002). Disadvantages, however, are the incapability to investigate insights of the structure as well as a destruction of the biofilm caused by the cantilever (Böl et al., 2013).

OCT could in future be used to link and understand differences of rheological experiments on the micro- and macroscale. Rheological experiments on the macroscale should be interpreted differently (Ochoa et al., 2007). Unlike experiments on the microscale, setups such as rotating disc rheometers do not investigate defined or individual biofilm structures, but rather a community and therefore an average of the rheological properties. Towler et al. (2003) conducted rotating disc rheometry experiments with multi-species biofilms. In their macroscale experiments a shear modulus ranging from $G = 0.3 - 45$ Pa was measured. This allows concluding that there is heterogeneity within the biofilm structure and between different biofilms. Thereby, a detailed examination of local structures as presented in this study is justified since the local biofilm characteristics merge in macroscale experiments. The shear moduli from different experiments vary over a wide range and are summarized in Böl et al. (2013). However experiments on the macroscale lack information of how the inner structure of the biofilm changes and influences mechanical stability and mass transfer. Properties such as porosity as well as biomass and cavity distribution have influence on structural stability and need to be considered. This was further investigated in time-lapsed measurements and is discussed in the following.

449 **Time-Lapsed Processes**

450 During the time-lapsed experiments the viscoelastic behavior of the biofilms was investigated.
451 While the mean biofilm thickness decreases as result of increasing shear stress, the biofilm did not
452 regain its initial structure after flow was stopped. Only 80 % of the initial biofilm thickness was
453 reached. Dreszer et al., (2014) showed that flow normal to the biofilm surface has a high impact on
454 biofilm compression in a lab-scale cross-flow membrane filtration applications. By enhancing the
455 permeate flux from 20 to 60 $L\,m^2\,h^{-1}$ for 1 h, followed by lowering to the original flux, they
456 measured a restore of the mean biofilm thickness of 75 %. Their result is thus in good agreement
457 with the results presented in this study. Application of shear stress during stress-strain experiments
458 caused filaments at the biofilm surface to attach onto the structure in order to adapt to the changed
459 flow and shear conditions. This is in agreement with the trend of the surface roughness coefficient,
460 which tents to decrease during increasing shear stress and *vice versa*. Movement of (filamentous)
461 structures or detachment had great impact on the surface roughness coefficient leading to a sort of
462 'steps' in the corresponding curve. The surface roughness coefficient calculated for C-scans was
463 higher than those for B-scans due to a greater variance in biofilm thickness within the captured
464 volume. This was mainly a result of the overall biofilm structure not covering the whole imaging
465 area. Space on the substratum that is not or barely covered reduced the calculated mean biofilm
466 thickness and hence led to a higher surface roughness coefficient compared to those calculated
467 from B-scans. For volumetric representations (C-scans) the biofilm porosity gives accurate values
468 to describe dynamics in the biofilm. As the biofilm is compressed, water will be excluded from
469 voids. The recovery of porosity during the decreasing shear stress supports that the biofilm did not
470 regain its original conformation. In consequence the adaption to further changing shear stress
471 conditions is influenced or restricted. While the biofilm porosity during elastic deformations

changed by $\Delta\Phi_{biofilm} = 2\,\%$, inelastic deformation showed a change of $\Delta\Phi_{biofilm} = 7\%$. This does not only influence the biofilm structure, but will also influence the diffusive transport of nutrients within the biofilm matrix. In several studies the effect of changing diffusion coefficients in biofilms grown at different flow velocities were demonstrated (Beyenal and Lewandowski, 2002; Brito and Melo, 1999). Brito and Melo (1999) showed with their experiments that an increase of the mass transfer coefficients by up to 20 % is possible. This is in agreement with dynamic 2D modeling approach introduced by Taherzadeh et al. (2012) who showed how mass transfer is influenced by moving biofilm streamers. Taherzadeh et al. (2012) calculated an increase in substrate uptake for the whole biofilm streamer of up to 20 % and even higher at the most oscillating streamer tip.

With OCT as presented in this communication, a link between the mesoscopic biofilm structure and the biofilm porosity could be shown. Furthermore, it is expected to be the main reasons for changes on mass transfer processes as well as on the viscoelastic deformation of biofilms. The estimated Young's Modulus *E* is in good agreement with other studies. Stoodley *et al.* (1999) for instance performed similar stress-strain experiments in flow cells and estimated an average Young's Modulus of $E = 40 \pm 8$ Pa for their biofilm compared to $E = 36 \pm 2.6$ Pa presented here. Stoodley *et al.* (1999) applied shear stress up to $\tau_w = 10$ Pa and showed the viscoelastic behavior of biofilms and additionally shear thickening for shear stresses over $\tau_w = 5$ Pa. Shear thickening was not detected in the current experiments, because the maximal shear stress applied was 3.6 Pa. The hysteresis in the stress-strain curves might also be a result of creep. However, Shaw et al. (2004) showed that there is a distinct time interval for elastic responses in biofilms. This is the time it takes for completely irreversible deformation. While biofilms in their studies

showed an average elastic response time of 18 min, the authors observed irreversible deformation also in shorter periods of time. Within the experiment presented here, shear stress applied over 30 min resulted still in an elastic response. Changes in strain might have been present, but did not exceed the lateral resolution of the OCT of 8.6 µm.

Conclusions

OCT is a versatile tool to investigate structural changes of biofilms *in situ* in 'real' time or in time-lapsed measurements. OCT B-scans are capable of capturing dynamic biofilm structure changes caused by a change in shear stress, while OCT C-scans provide additional information about the viscoelastic behavior and how parameters such as porosity or surface roughness influence the mechanical stability of biofilms. The non-invasive and *in situ* visualization of biofilms at the mesoscale offers the possibility of calculating rheological properties such as the shear modulus G or the Young's Modulus E as well as geometrical changes such as the angle of deformation α, elongation ΔL, and strain ε to describe the biofilm structure and its changes. The shear modulus G as well as Young's Modulus E have been estimated on a similar level compared to other studies. Moreover, viscoelasticity has been shown in stress-strain experiments and was in good agreement with values reported in literature. The fast scanning speed of OCT allows to acquire images in 2D and 3D without destroying the biofilm structure. Furthermore, OCT reveals insights about the biofilm structure and will thus help to better understand the formation and maturing of biofilm structures as well as capture the dynamics of the initial behavior of biofilms under suddenly changing shear stress conditions. An interesting application of OCT could thus be the quantification of dental plaque and the effect of the cleaning device on the dental biofilm (Busscher et al., 2010).

As a proof of concept we showed that OCT is a powerful imaging technique, which additionally allows quantifying biofilm rheology in dynamic and time-lapsed experiment to complete the understanding of the interaction between structural properties and rheological behavior.

Acknowledgments

This work was funded by the European Commission grant 611640. For the technical advice and manufacture of the flow cells we would like to thank Stefan Giselbrecht from the Institute for Biological Interfaces at the Karlsruhe Institute of Technology. The authors would also very much like to thank all reviewers for their contributions and mindful advices improving the manuscript.

References

Beech IB, Smith JR, Steele AA, Penegar I, Campbell SA. 2002. The use of atomic force microscopy for studying interactions of bacterial biofilms with surfaces. *Colloids Surfaces B Biointerfaces* **23**:231–247.

Beyenal H, Lewandowski Z. 2002. Internal and external mass transfer in biofilms grown at various flow velocities. *Biotechnol. Prog.* **18**:55–61.

Böl M, Ehret AE, Bolea Albero A, Hellriegel J, Krull R. 2013. Recent advances in mechanical characterisation of biofilm and their significance for material modelling. *Crit. Rev. Biotechnol.* **33**:145–71.

Brito AG, Melo LF. 1999. Mass transfer coefficients within anaerobic biofilms: Effects of external liquid velocity. *Water Res.* **33**:3673–3678.

Brooun A, Liu S, Lewis K. 2000. A Dose-Response Study of Antibiotic Resistance in Pseudomonas aeruginosa Biofilms. *Antimicrob. Agents Chemother.* **44**:640–646.

Busscher H, Jager D, Finger G, Schaefer N, HC van der M. 2010. Energy transfer , volumetric expansion , and removal of oral biofilms by non-contact brushing **118**:177–182.

539 Christensen BE, Characklis WG. 1990. Physical and chemical properties of biofilms. In:
540 Characklis, WG, Marshall, KC, editors. *Biofilms*. New York: John Wiley & Sons, pp. 93–
541 130.

542 Dreszer C, Wexler AD, Drusová S, Overdijk T, Zwijnenburg A, Flemming H-C, Kruithof JC,
543 Vrouwenvelder JS. 2014. In-situ biofilm characterization in membrane systems using
544 Optical Coherence Tomography: Formation, structure, detachment and impact of flux
545 change. *Water Res.* **67**:243–254.

546 Drexler W, Fujimoto JG. 2008. Optical Coherence Tomography: Technology and Applications.
547 Ed. W Drexler, James G Fujimoto 1st ed. Berlin, Heidelberg, New York: Springer-Verlag.

548 Flemming H-C, Wingender J. 2010. The biofilm matrix. *Nat. Rev. Microbiol.* **8**:623–33.

549 Guélon T, Mathias J-D, Stoodley P. 2011. Advances in Biofilm Mechanics. In: Flemming, H-C,
550 Wingender, J, Szewzyk, U, editors. *Biofilm Highlights*. Berlin, Heidelberg: Springer-Verlag.
551 Springer Series on Biofilms, Vol. 5, pp. 111–139.

552 Haisch C, Niessner R. 2007. Visualisation of transient processes in biofilms by optical coherence
553 tomography. *Water Res.* **41**:2467–72.

554 He Y, Peterson BW, Jongsma M a, Ren Y, Sharma PK, Busscher HJ, van der Mei HC. 2013.
555 Stress relaxation analysis facilitates a quantitative approach towards antimicrobial
556 penetration into biofilms. *PLoS One* **8**:e63750.

557 Hu Z, Luo H, Du Y, Lu H. 2013. Fluorescent stereo microscopy for 3D surface profilometry and
558 deformation mapping. *Opt. Express* **21**:11808–18.

559 Huang D, Swanson E, Lin C, Schuman J, Stinson W, Chang W, Hee M, Flotte T, Gregory K,
560 Puliafito C, Et A. 1991. Optical coherence tomography. *Science (80-.).*

561 Klapper I, Rupp CJ, Cargo R, Purvedorj B, Stoodley P. 2002. Viscoelastic fluid description of
562 bacterial biofilm material properties. *Biotechnol. Bioeng.* **80**:289–96.

563 Körstgens V, Flemming H-C, Wingender J, Borchard W. 2001. Uniaxial compression
564 measurement device for investigation of the mechanical stability of biofilms. *J. Microbiol.*
565 *Methods* **46**:9–17.

566 Lawrence JR, Korber DR, Hoyle BD, Costerton JW, Caldwell DE. 1991. Optical sectioning of
567 microbial biofilms. *J. Bacteriol.* **173**:6558–67.

568 Möhle RB, Langemann T, Haesner M, Augustin W, Scholl S, Neu TR, Hempel DC, Horn H.
569 2007. Structure and shear strength of microbial biofilms as determined with confocal laser

570 scanning microscopy and fluid dynamic gauging using a novel rotating disc biofilm reactor.
571 *Biotechnol. Bioeng.* **98**:747–55.

572 Morgenroth E, Milferstedt K. 2009. Biofilm engineering: linking biofilm development at
573 different length and time scales. *Rev. Environ. Sci. Bio/Technology* **8**:203–208.

574 Murga R, Stewart PS, Daly D. 1995. Quantitative analysis of biofilm thickness variability.
575 *Biotechnol. Bioeng.* **45**:503–10.

576 Ochoa J-C, Coufort C, Escudié R, Liné A, Paul E. 2007. Influence of non-uniform distribution of
577 shear stress on aerobic biofilms. *Chem. Eng. Sci.* **62**:3672–3684.

578 Otsu N. 1979. A Threshold Selection Method from Gray-Level Histograms. *IEEE Trans. Syst.*
579 *Man. Cybern.* **9**:62–66.

580 Peulen T-O, Wilkinson KJ. 2011. Diffusion of nanoparticles in a biofilm. *Environ. Sci. Technol.*
581 **45**:3367–73.

582 Rupp CJ, Fux CA, Stoodley P. 2005. Viscoelasticity of Staphylococcus aureus biofilms in
583 response to fluid shear allows resistance to detachment and facilitates rolling migration.
584 *Appl. Environ. Microbiol.* **71**:2175–8.

585 Schneider CA, Rasband WS, Eliceiri KW. 2012. NIH Image to ImageJ: 25 years of image
586 analysis. *Nat. Methods* **9**:671–675.

587 Shaw T, Winston M, Rupp CJ, Klapper I, Stoodley P. 2004. Commonality of Elastic Relaxation
588 Times in Biofilms. *Phys. Rev. Lett.* **93**:098102.

589 Spoering AL, Lewis K. 2001. Biofilms and planktonic cells of Pseudomonas aeruginosa have
590 similar resistance to killing by antimicrobials. *J. Bacteriol.* **183**:6746–51.

591 Stoodley P, Hall-Stoodley L, Lappin-Scott HM. 2001. Detachment, surface migration, and other
592 dynamic behavior in bacterial biofilms revealed by digital time-lapse imaging. *Methods*
593 *Enzymol.* **337**:306–19.

594 Stoodley P, Lewandowski Z, Boyle JD, Lappin-Scott HM. 1999. Structural deformation of
595 bacterial biofilms caused by short-term fluctuations in fluid shear: an in situ investigation of
596 biofilm rheology. *Biotechnol. Bioeng.* **65**:83–92.

597 Taherzadeh D, Picioreanu C, Horn H. 2012. Mass transfer enhancement in moving biofilm
598 structures. *Biophys. J.* **102**:1483–92.

599 Taherzadeh D, Picioreanu C, Simone A, Wall WA, Horn H, Küttler U. 2010. Computational
600 study of the drag and oscillatory movement of biofilm streamers in fast flows. *Biotechnol.*
601 *Bioeng.* **105**:600–610.

602 Towler BW, Rupp CJ, Cunningham AB, Stoodley P. 2003. Viscoelastic properties of a mixed
603 culture biofilm from rheometer creep analysis. *Biofouling* **19**:279–85.

604 Wagner M, Taherzadeh D, Haisch C, Horn H. 2010. Investigation of the mesoscale structure and
605 volumetric features of biofilms using optical coherence tomography. *Biotechnol. Bioeng.*
606 **107**:844–53.

607 Xi C, Marks D, Schlachter S, Luo W, Boppart S. 2006. High-resolution three-dimensional
608 imaging of biofilm development using optical coherence tomography. *J. Biomed. Opt.*
609 **11**:34001.

610 Yoo BK, Chen J. 2012. Role of cellulose in protecting Shiga toxin producing Escherichia coli
611 against oxidative and acidic stress. *Food Control* **23**:289–292.

612

613

Figure Captions

Figure 1: **A** Scheme of the flow cell setup for biofilm cultivation and OCT measurements. Images were taken from biofilm colonies grown in the middle of the flow channel. **B** The principle of the spectral domain OCT is a Michelson interferometer setup with a broadband super luminescent diode (SLD), a beam splitter, and a fixed reference mirror. Two scanning mirrors in the sample arm allow to create a depth scan (A-scan), a cross section of the biofilm (B-scan) or a volumetric representation (C-scan).

Figure 2: Brightness enhanced B-scan from the first shear stress experiment at $\tau_w = 0.8$ Pa. The image shows the maximal deformation along the axis of flow. The white line represents the structure before the flow started and the deposition and structural change of the two largest voids. Scale bar equals 250 µm.

Figure 3: Brightness enhanced B-scans. The montage displays every second B-scan of the second shear stress experiment. Steady mean biofilm thickness occurred between B-scan 600 ms and 1300 ms. Within the final image at 2100 ms the shape of the original biofilm structure is represented by the white line. Scale bar equals 250 µm.

Figure 4: **A** Plot of the mean biofilm thickness varying over time. The mean biofilm thickness $\bar{L}_F$ of the total structure (crosses ×) shows a plateau between B-scan 600 ms and 1300 ms, indicated by the grey area, as a result of a difference in compression of the upstream half (filled circle •) and downstream half (empty circle ◦). **B** shows the plot of the surface roughness coefficient R_a^* over time. The biofilm roughness coefficient R_a^* shows a linear slope, which is reduced at the beginning of the steady biofilm thickness, indicated by the grey area.

Figure 5: Brightness enhanced OCT B-scans of the biofilm deformation as a function of the shear stress τ_w from the beginning and the end of the experiment. **A** shows the OCT B-scan at 0 ms under growth conditions τ_w = 0.01 Pa while **B** shows OCT B-scan at 2100 ms, after changing the shear stress to τ_w = 1.64 Pa. The filamentous structure elongated due to the shear stress (ΔL = 220 µm). Simultaneously a change of the angle of deformation α = 3° was observed. Scale bar equals 250 µm. Flow from left to right.

Figure 6: Deformation of the of the biofilm structure in a time-lapsed experiment. A shear stress of $\tau_w = 1.64$ Pa was applied for 30 min and consecutive relaxation was monitored over 20 min. A maximal angle of deformation $\alpha = 3°$ was detected within 1 min and did not change until the flow was stopped. The biofilm showed elastic response by returning into its original conformation after 50 minutes. Scale bar equals 250 µm. Flow from left to right.

Figure 7: **A** Plot of the volumetric biofilm porosity changing over time in a time-lapsed deformation measurement. The porosity of the volumetric representation equaled $\Phi_{\text{biofilm}} = 51\ \%$ at the beginning of the experiment. It decreased by $\Delta\Phi_{\text{biofilm}} = 7\%$ during the loading cycle and regained a porosity of $\Phi_{biofilm} = 46\ \%$ at the end of the experiment. **B** Plot of the volumetric surface roughness coefficient over time. The biofilm surface roughness decreased during the load cycle and increased during the unload cycle. The steps are a result of biofilm detachment.

Figure 8: Cross section from the volumetric representation. The image shows the biofilm after the stress-strain experiments at $\tau_w = 0$ Pa while the white line represents the biofilm structure from

654 the beginning of the experiment. The image shows the viscoelastic deformation in the front half
655 and the detachment in the rear half. Scale bar equals 250 μm. Flow from left to right.

656 **Figure 9**: **A** Plot of the mean biofilm thickness during a stress-strain experiment. The viscoelastic
657 behavior can directly be related to the reduced biofilm thickness after the experiment. **B** Stress-
658 strain curve also shows the viscoelastic biofilm deformation. The hysteresis is directly related to
659 viscoelastic properties of the biofilm. From the linear part during the load cycle the Young's
660 modulus E was estimated to be $E = 36.0 \pm 2.6$ Pa via least squares fit.

figure 1

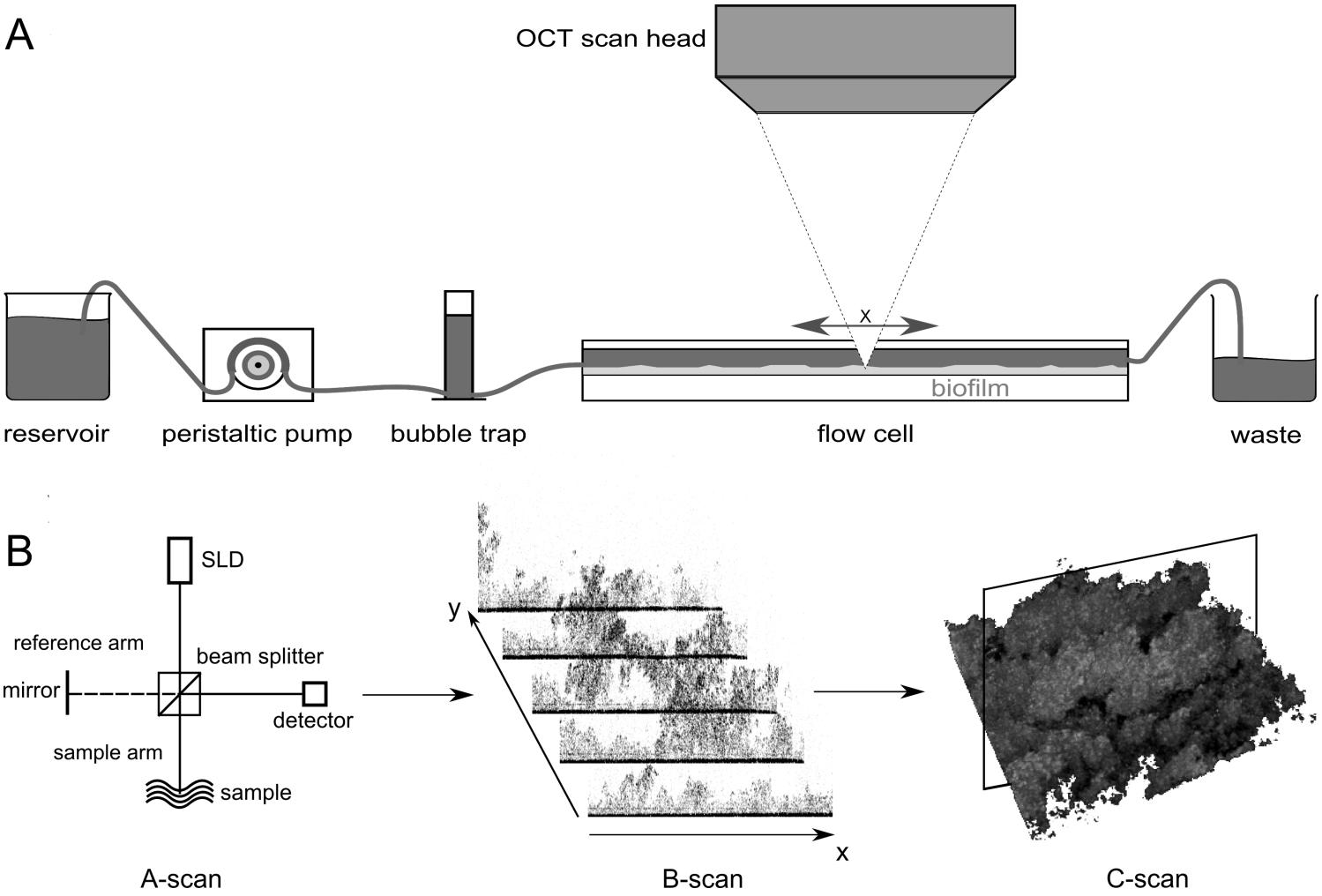
A
OCT scan head
x
biofilm
reservoir
peristaltic pump
bubble trap
flow cell
waste
B
SLD
reference arm
beam splitter
mirror
detector
sample arm
sample
y
x
A-scan
B-scan
C-scan

figure 2

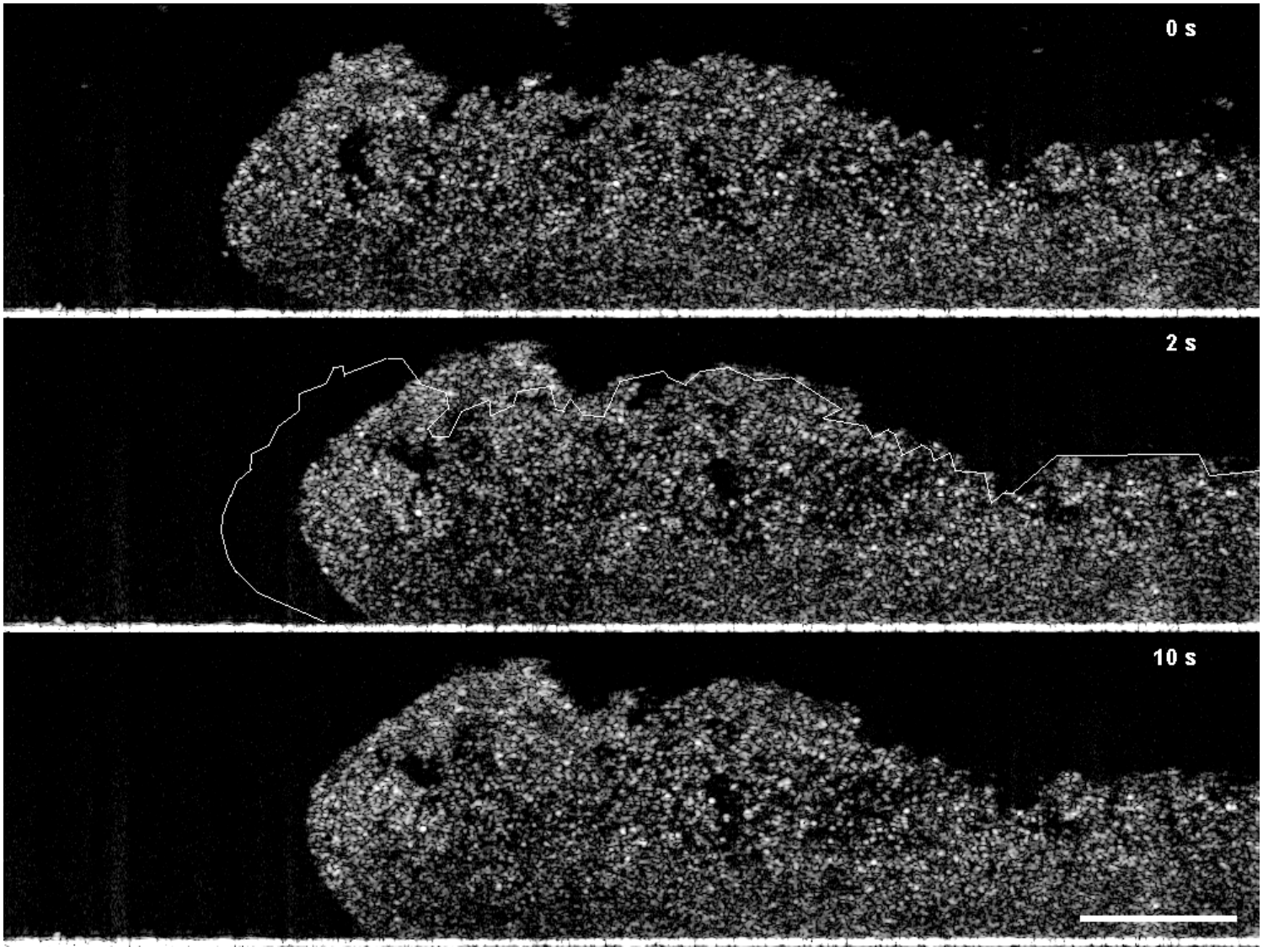

figure 3

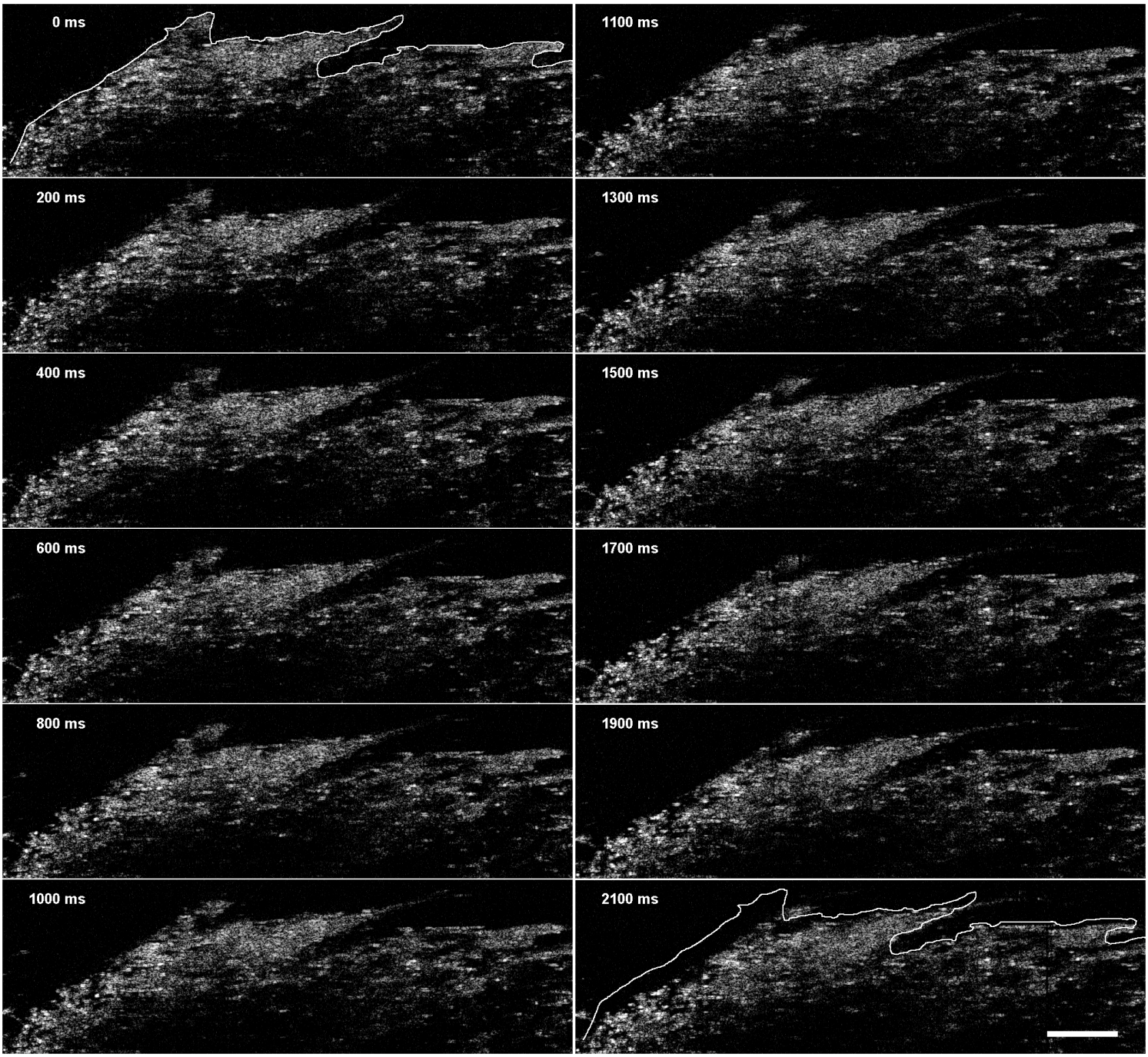
0 ms
1100 ms
200 ms
1300 ms
400 ms
1500 ms
600 ms
1700 ms
800 ms
1900 ms
1000 ms
2100 ms

figure 4

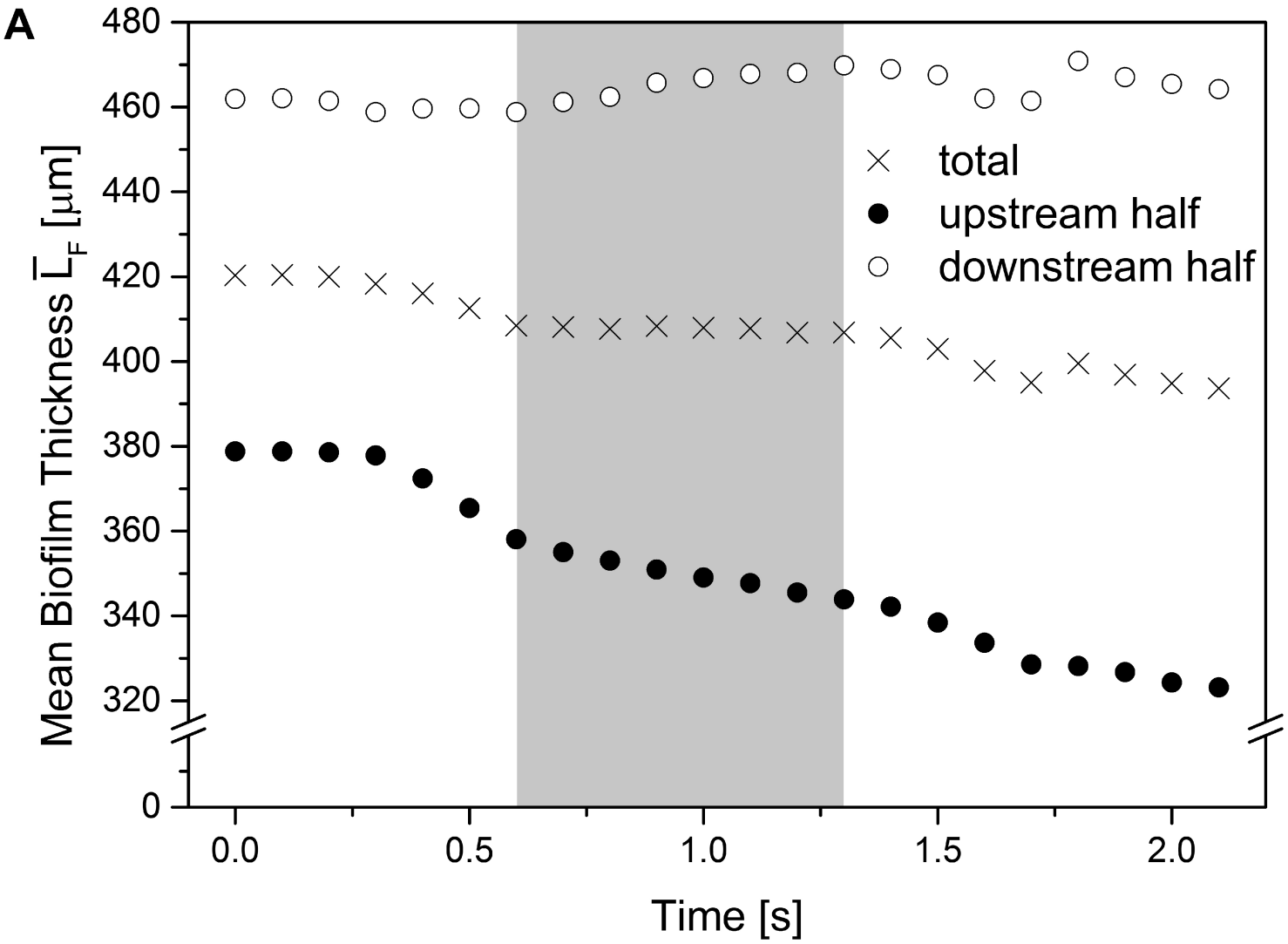
A
480
460
440
420
400
380
360
340
320
0
Mean Biofilm Thickness $\bar{L}_F$ [µm]
total
upstream half
downstream half
0.0
0.5
1.0
1.5
2.0
Time [s]

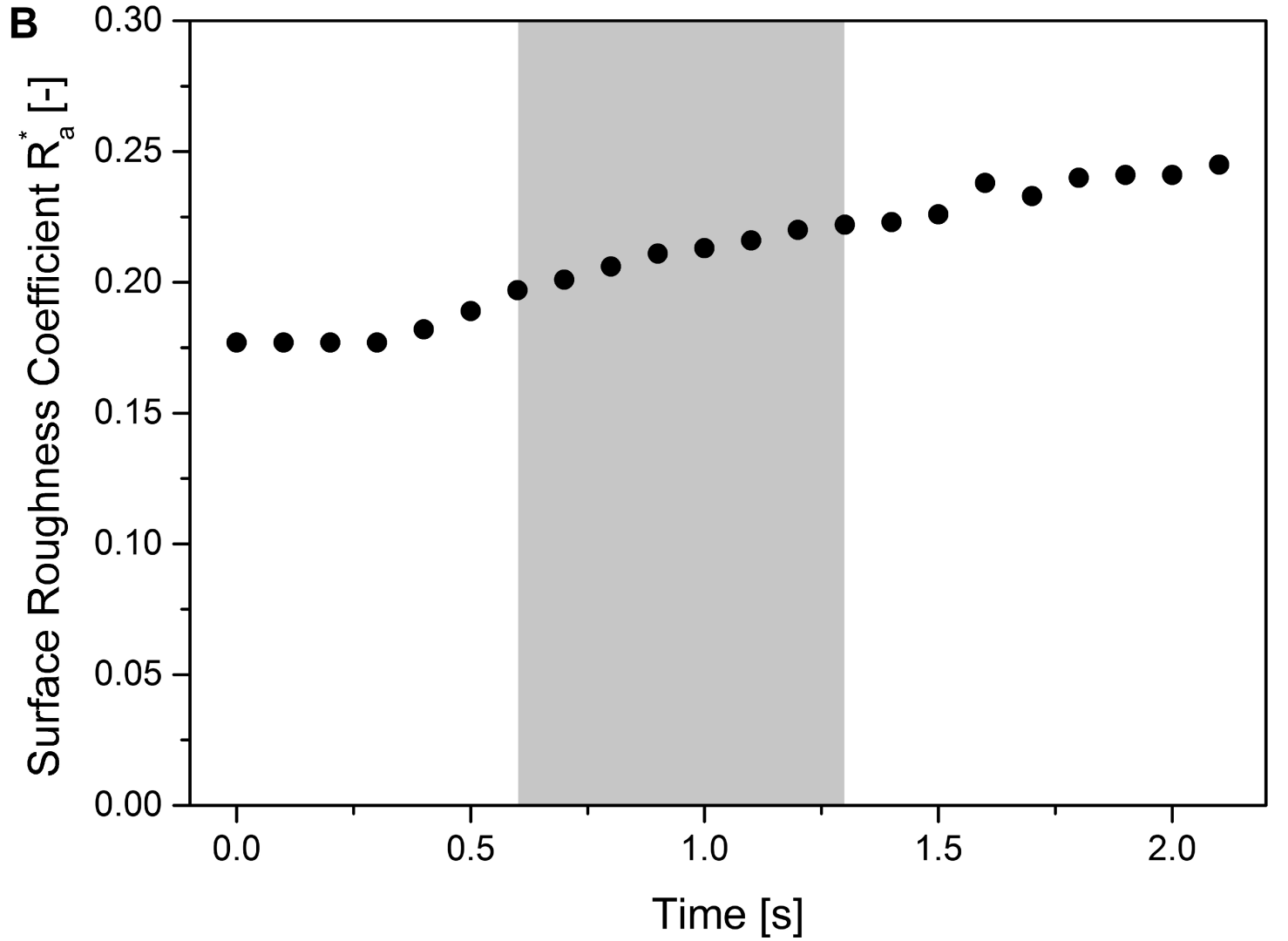
B
0.30
0.25
0.20
0.15
0.10
0.05
0.00
Surface Roughness Coefficient R_a^* [-]
0.0
0.5
1.0
1.5
2.0
Time [s]

figure 5

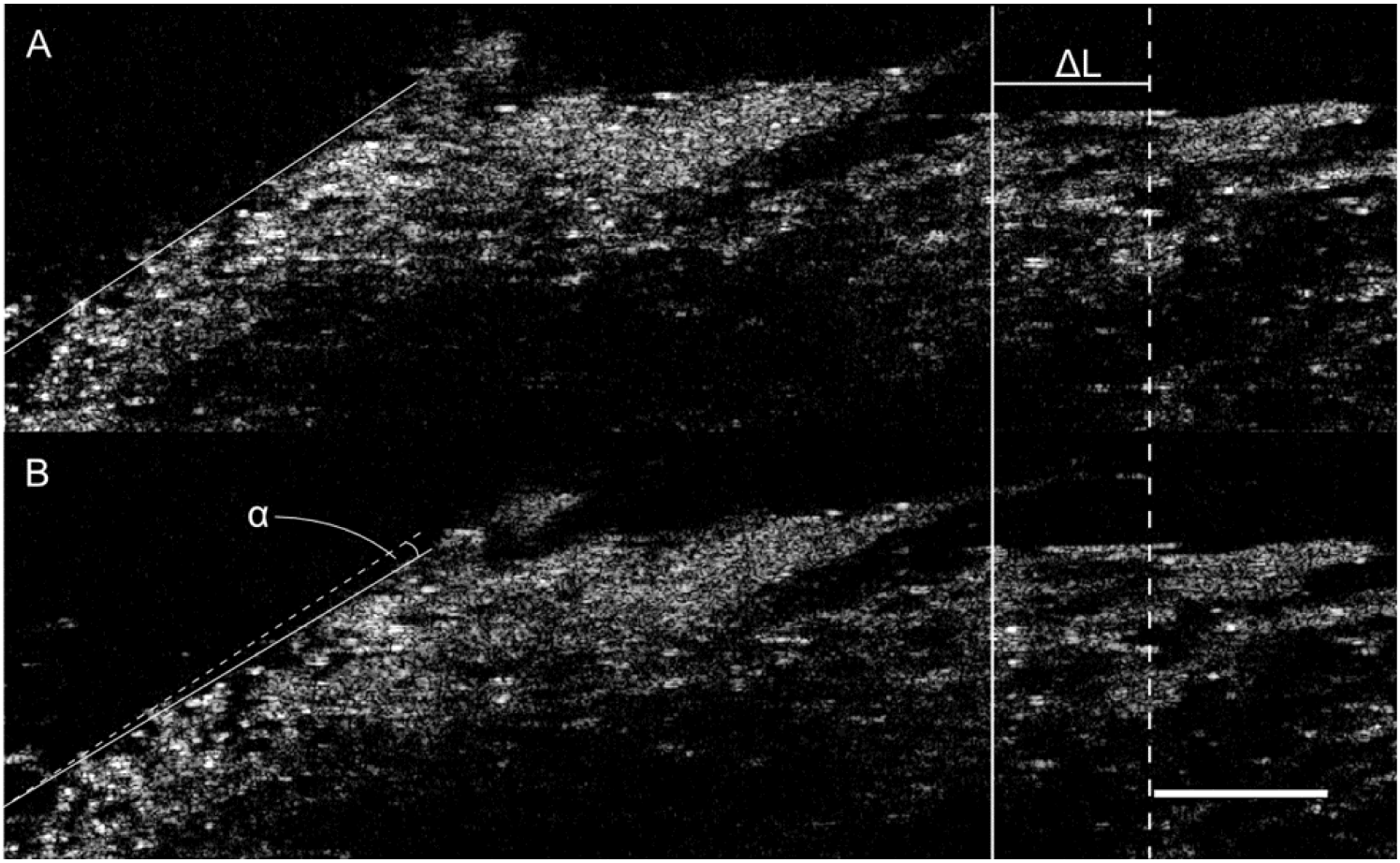

figure 6

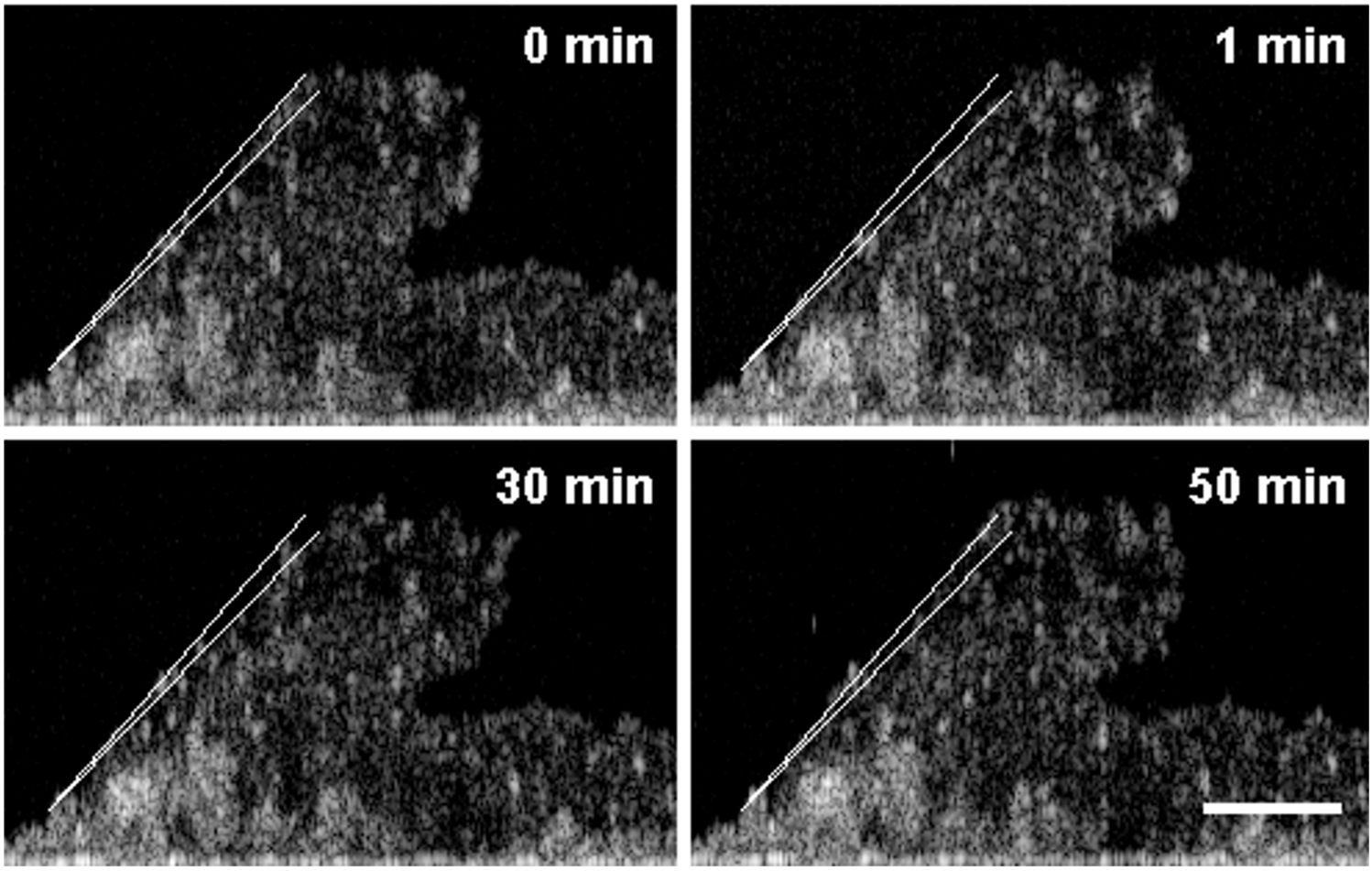

figure 7

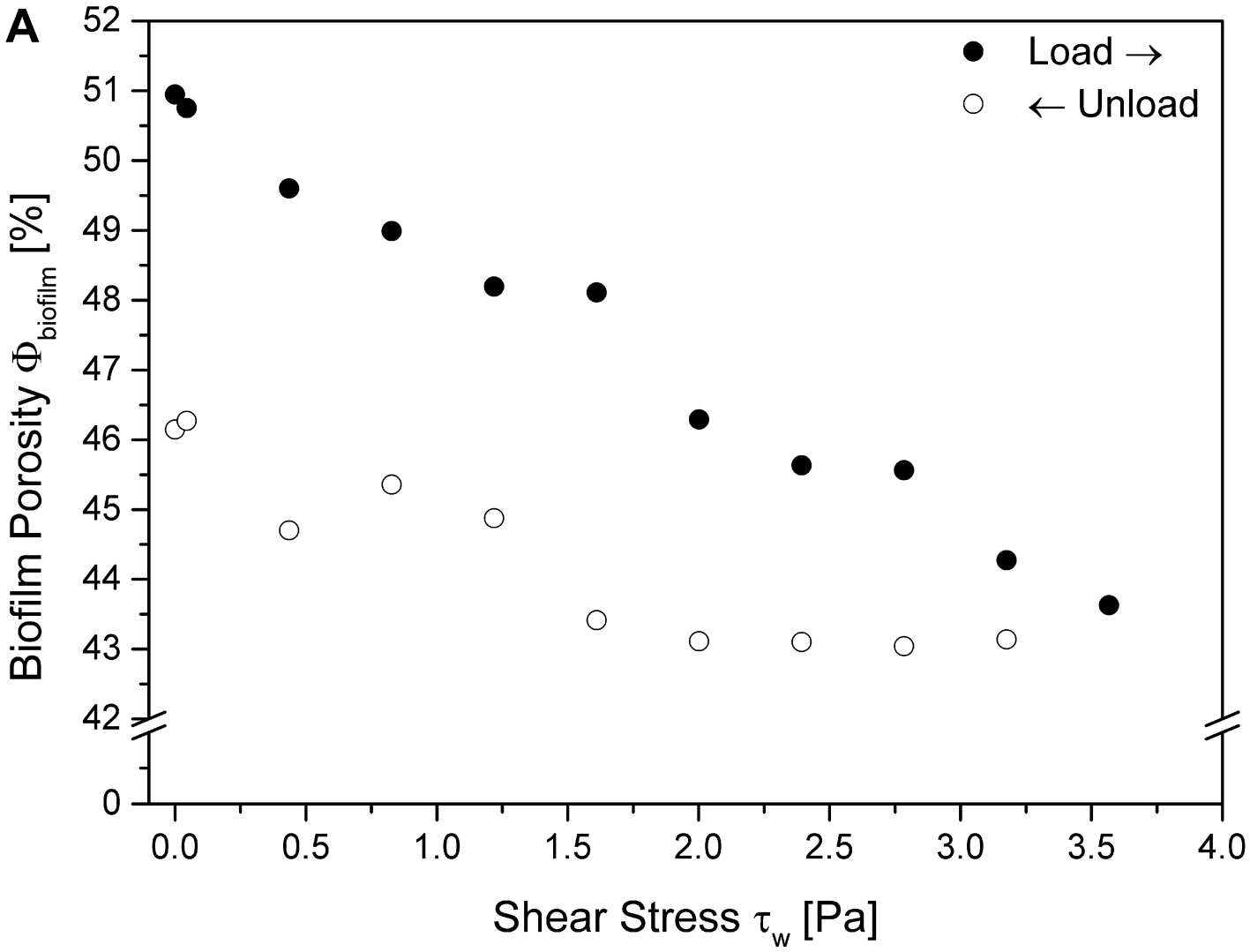
A
Load →
← Unload
Biofilm Porosity $\Phi_{biofilm}$ [%]
52
51
50
49
48
47
46
45
44
43
42
0
0.0
0.5
1.0
1.5
2.0
2.5
3.0
3.5
4.0
Shear Stress τ_w [Pa]

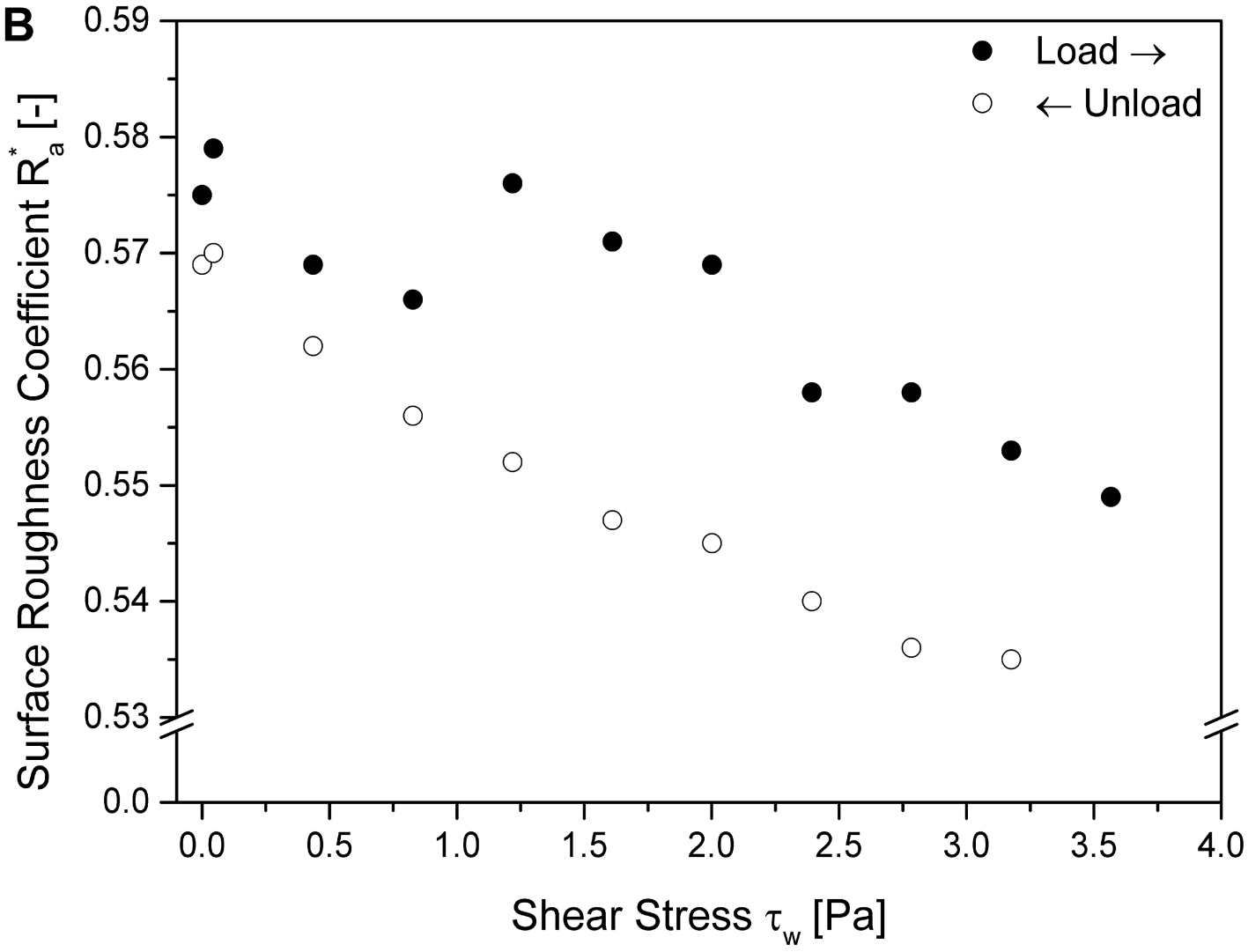
B
Load →
← Unload
Surface Roughness Coefficient R_a^* [-]
0.59
0.58
0.57
0.56
0.55
0.54
0.53
0.0
0.0
0.5
1.0
1.5
2.0
2.5
3.0
3.5
4.0
Shear Stress τ_w [Pa]

figure 8

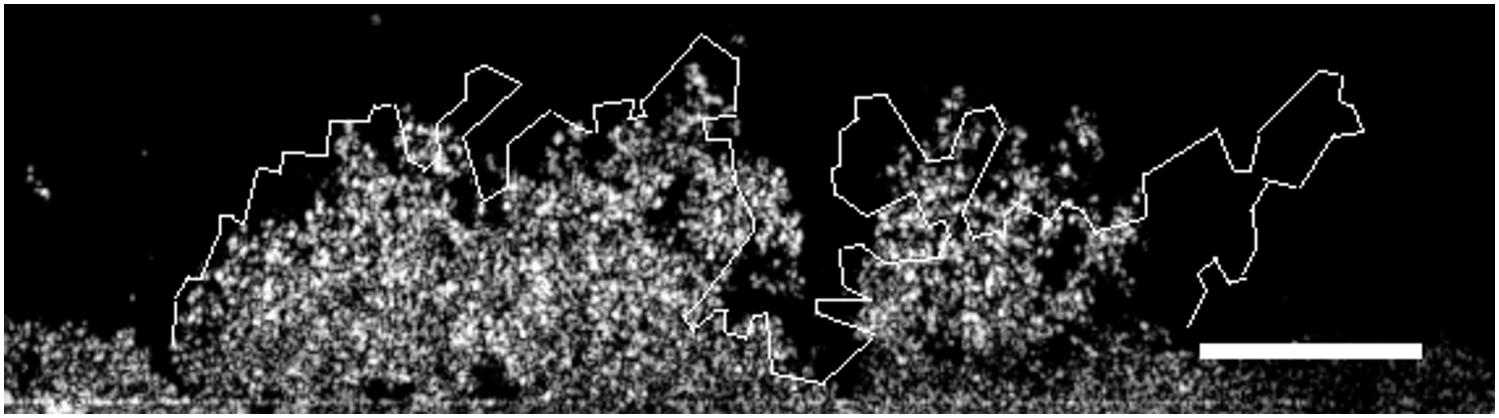

figure 9

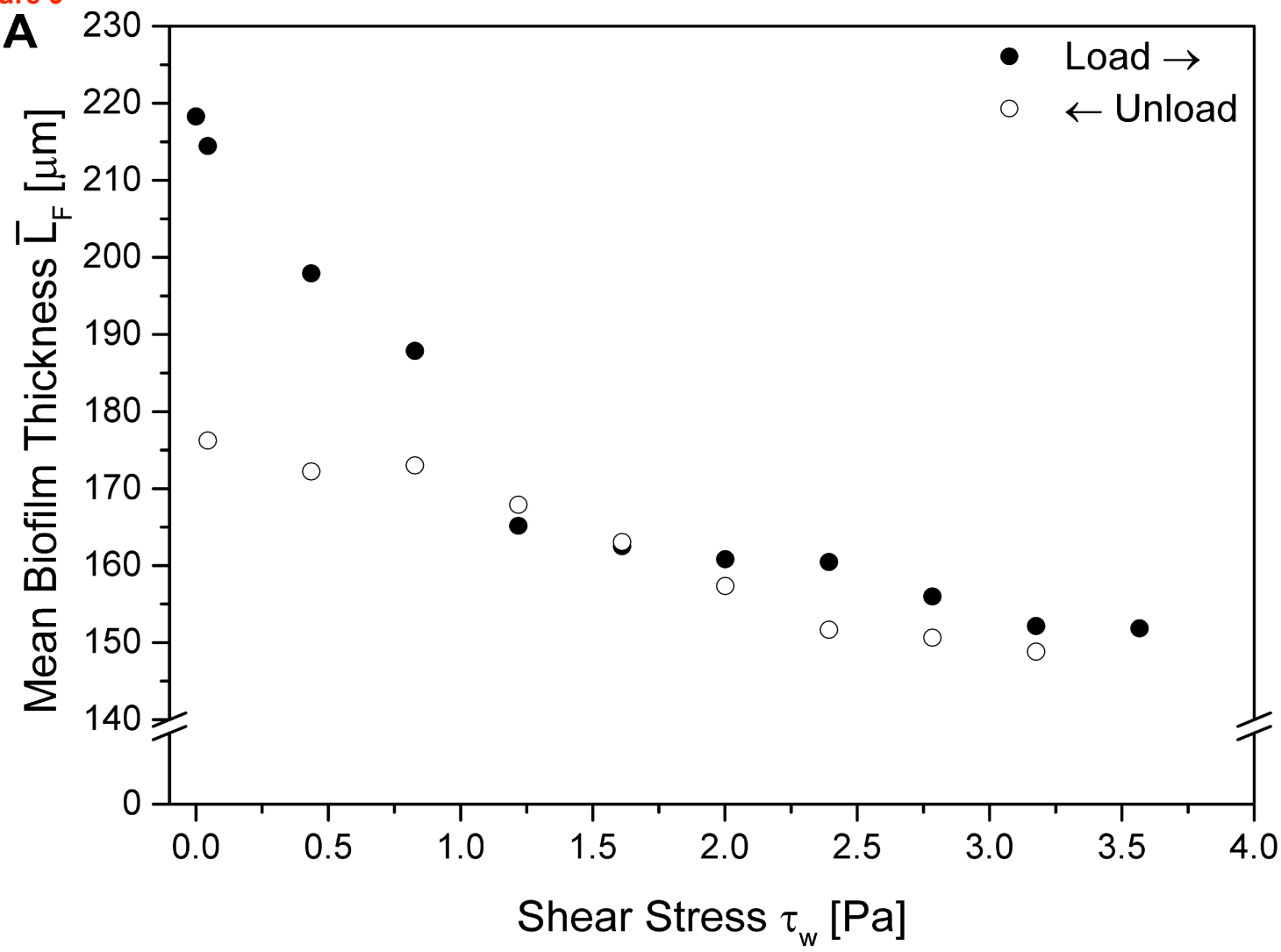
A
Load →
← Unload
Mean Biofilm Thickness $\bar{L}_F$ [µm]
230
220
210
200
190
180
170
160
150
140
0
0.0
0.5
1.0
1.5
2.0
2.5
3.0
3.5
4.0
Shear Stress τ_w [Pa]

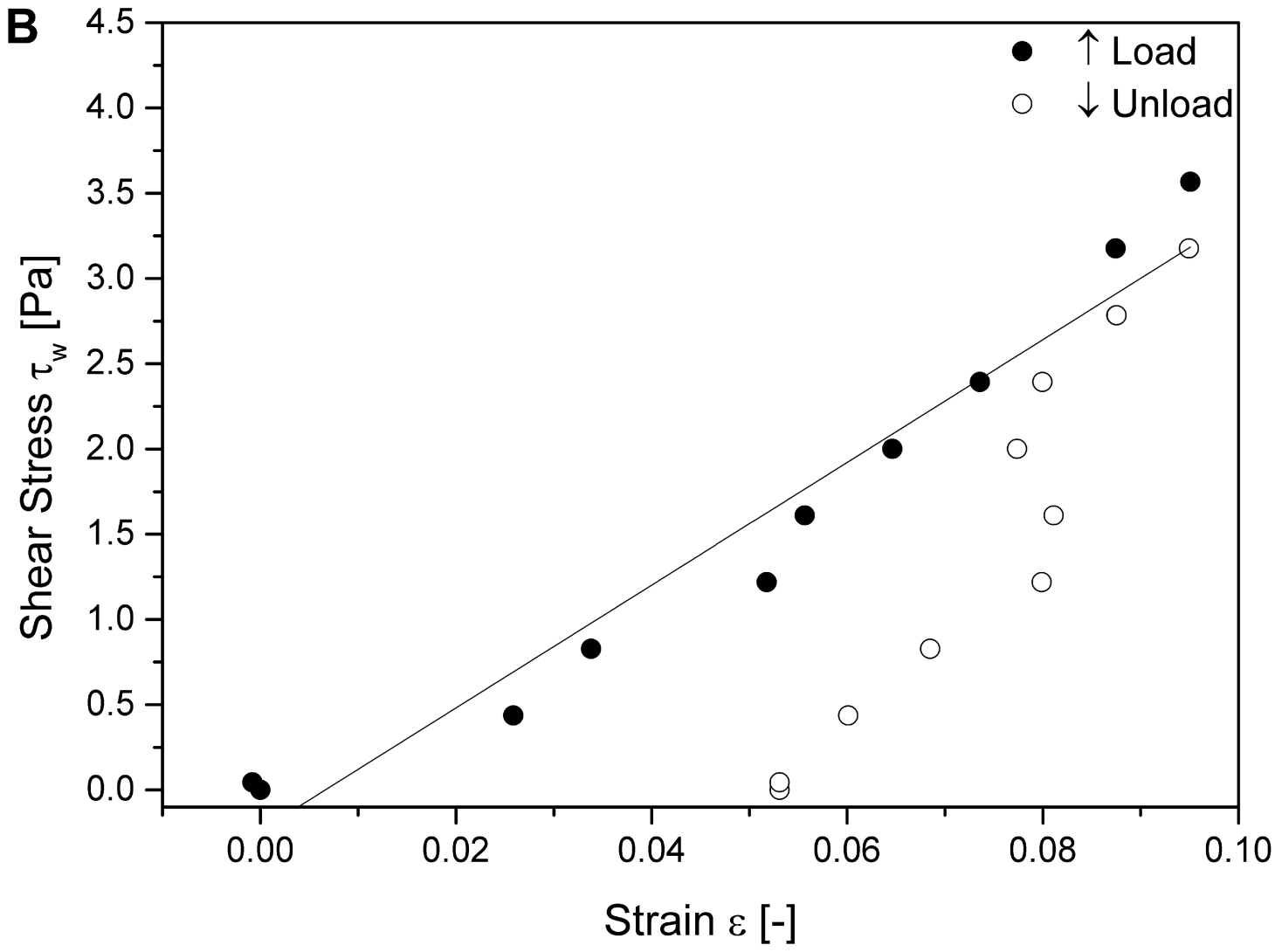
B
↑ Load
↓ Unload
Shear Stress τ_w [Pa]
4.5
4.0
3.5
3.0
2.5
2.0
1.5
1.0
0.5
0.0
0.00
0.02
0.04
0.06
0.08
0.10
Strain ε [-]